Journal of Alloys and Compounds 806 (2019) 1029–1038

Contents lists available at ScienceDirect

Journal of Alloys and Compounds

journal homepage: http://www.elsevier.com/locate/jalcom

Hierarchical (Ni,Co)Se_2/CNT hybrid microspheres consisting of a porous yolk and embossed hollow thin shell for high-performance anodes in sodium-ion batteries

Se Hwan Oh, Jung Sang Cho*

Department of Engineering Chemistry, Chungbuk National University, Chungbuk, 361-763, Republic of Korea

ARTICLE INFO

Article history:
Received 29 April 2019
Received in revised form
16 July 2019
Accepted 29 July 2019
Available online 30 July 2019

Keywords:
Yolk-shell
Spray pyrolysis
Sodium-ion batteries
Anodes
(Ni,Co)Se_2

ABSTRACT

Hierarchical yolk-shell-structured $NiCoSe_2$/CNT [HYS-(NiCo)Se_2/CNT] hybrid microspheres consisting of a porous yolk and embossed hollow thin shell were prepared by one-step spray pyrolysis and subsequent selenization heat treatment for potential use as anode materials for sodium-ion batteries. The unique HYS-(NiCo)Se_2/CNT microspheres had a hierarchical configuration of an external thin shell, inside porous yolk, and interstitial hollow space. In particular, the porous yolk is composed of CNTs walls and contained interconnected mesopores formed by PS decomposition during one-step spray pyrolysis. The discharge capacity of the HYS-(NiCo)Se_2/CNT microspheres was 366 mA h g^{-1} after 10,000 cycles at a high current density of 3.0 A g^{-1}, and their capacity retention after the 2nd cycle was 85%. The HYS-(NiCo)Se_2/CNT microspheres have discharge capacities of 444, 429, 400, 380, 352, 329, 300, 266, 222, and 163 mA h g^{-1} at current densities of 0.5, 1.0, 2.0, 3.0, 5.0, 7.0, 10.0, 12.0, 15.0 and 20.0 A g^{-1}, respectively. The synergistic effects of the uniquely hierarchical yolk-shell structure, CNTs walls with high electrical conductivity, interstitial mesopores, and anchored (Ni,Co)Se_2 nanoparticles resulted in high structural stability during the cycles and excellent sodium-ion storage performance.

1. Introduction

Among energy-storage devices, sodium-ion batteries (SIBs) have been regarded as the most likely substitute for lithium-ion batteries (LIBs) because of their abundant reserves in the earth, low cost, and the hypotoxicity of sodium [1–3]. However, the larger ionic radius and molar mass of Na ions compared to those of Li ions give rise to the low reversible capacity of the cell induced by the high polarization and rapid capacity fading during Na-ion insertion and extraction [4–6]. In order to solve these problems, many nanostructuring strategies and numerous transitional-metal compounds (TMCs) have been investigated as anodes in SIBs [7–9]. In particular, the methods to control the structure, size, and morphologies of the TMCs as anodes and their hybrids with carbonaceous materials, such as graphite, carbon nanotubes (CNT), and graphene, have been considered to be the most likely to be good anodes [10–13]. The nanostructured carbon composited with anodes provides ample Na-ion storage sites, a large area that contacts the electrolyte, and a short path length of the Na ions and electrons, and can accommodate strain during cycling, thereby improving the electrochemical performance and cycling life of NIBs [14–16].

Recently, Jo et al. [17]. synthesized hierarchical yolk-shell-structured NiO/C hybrid microspheres for the first time. They are composed of a porous yolk with well-defined mesopores, a shell, and a hollow space between the yolk and shell. Both the phase separation of polyvinylpyrrolidone from polystyrene (PS) nanobeads containing a colloidal solution and the subsequent decomposition of PS nanobeads in the droplet during spray pyrolysis play key roles in the synthesis of the unique hierarchical yolk-shell structure. Therefore, the unique nanostructure showed superior energy-storage properties when applied to the anodes for LIBs.

Transitional-metal selenides (TMS) have also been studied widely and these show good characteristics for being anode materials in NIBs [7–9]. However, the synthetic method for the nanostructured TMS materials for SIBs are mostly limited to liquid phase processes, such as hydrothermal, precipitation, and emersion processes [18–20]. These processes for TMS nanostructures are generally time consuming and lack homogeneity for large-scale processing. Therefore, an easy scalable process useable for structural design of nanostructured TMS microspheres with uniform size distribution, interconnected pores, and high electrical conductivity has to be efficiently applied to make anode materials for

* Corresponding author.
E-mail address: jscho@cbnu.ac.kr (J.S. Cho).

https://doi.org/10.1016/j.jallcom.2019.07.351
0925-8388/

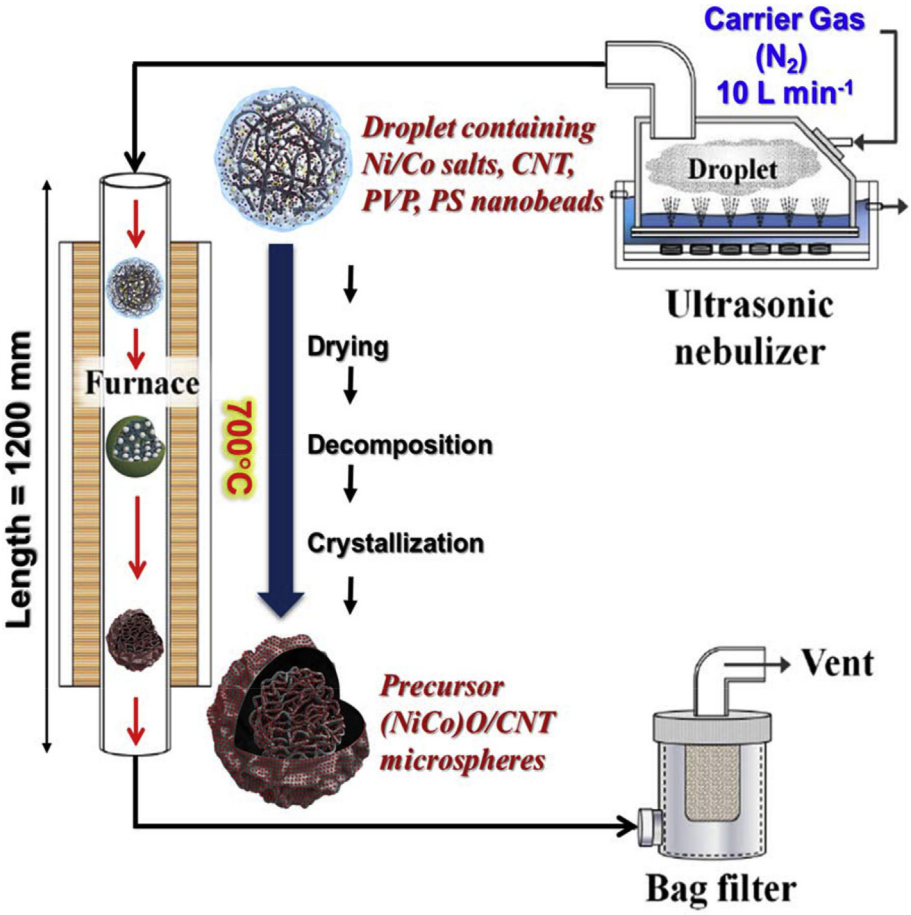

Scheme 1. Scheme of the spray pyrolysis process for the preparation of the precursor powders.

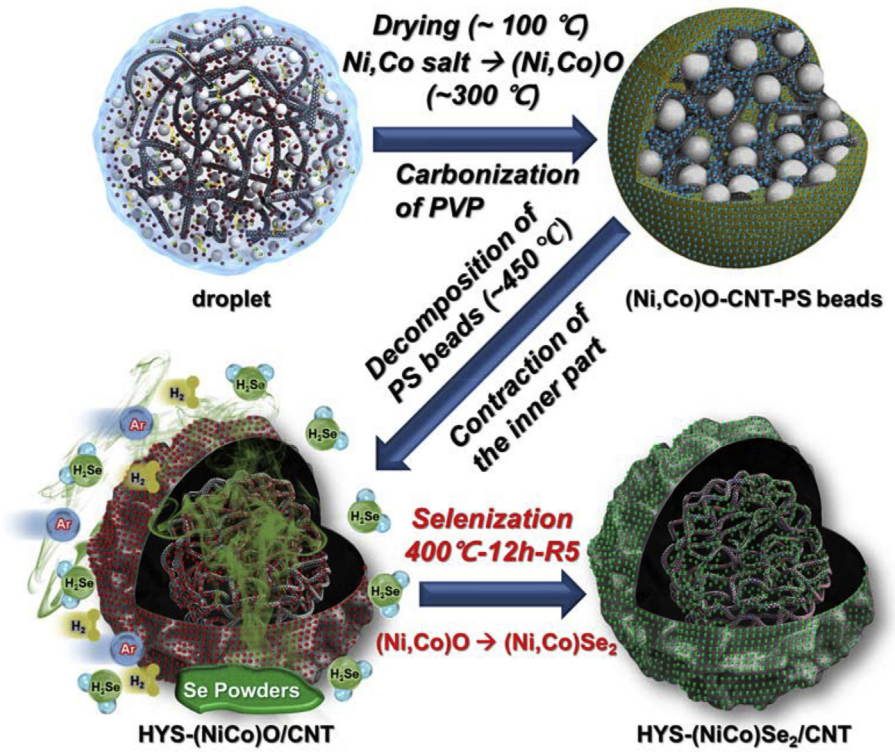

Scheme 2. Formation mechanism of HYS-(NiCo)Se_2/CNT microspheres by spray pyrolysis and subsequent selenization process.

SIBs.

Spray pyrolysis is a facile and cost-effective process that has been applied to prepare carbon composited microspheres with various compositions. Additionally, spray pyrolysis is advantageous as a nanostructuring strategy for powders, because different mechanisms could be applied by adding additives to the spray solution and controlling the process parameters during the process in a hot-wall reactor that yields a homogeneous composition.

In this study, hierarchical yolk-shell-structured $NiCoSe_2$/CNT [HYS-(NiCo)Se_2/CNT] hybrid microspheres consisting of a porous yolk and embossed hollow thin shell were successfully prepared by one-step spray pyrolysis and a subsequent facile heat-treatment process. Although single-phased metal selenides have been studied as anode materials for SIBs, binary TMS materials, $NiCoSe_2$ in this study, have rarely been studied. Binary transition metal compounds which have good electrical conductivity and high chemical and thermal stabilities have been proposed as promising anode materials [21–23]. Moreover, better capacity and cycling stability of anodes can be achieved when two transition metals are incorporated into the host layer [21–23]. In particular, binary Ni–Co compounds have received research attention owing to their high redox activities and because the Ni and Co nanoparticles formed during the reduction process act as catalysts for the reversible conversion of Na_2Se. Moreover, most studies of the yolk-shell-structured microspheres have been limited to transition-metal oxides and sulfides. In particular, the unique yolk-shell structure introduced in this study has an especially porous yolk with CNTs walls, which has not been studied for anodes in NIBs. The unique nanostructure is expected to provide efficient anode materials for SIBs with superior Na-ion storage performances.

2. Experimental section

2.1. Sample preparation

The hierarchical yolk-shell-structured $NiCoSe_2$/CNT [HYS-(NiCo)Se_2/CNT] hybrid microspheres were prepared by one-step spray pyrolysis and subsequent selenization heat treatment. The precursor powders were obtained by spray pyrolysis from a solution with 0.055 M nickel(II) nitrate tetrahydrate [$Ni(NO_3)_2 \cdot 6H_2O$, Junsei, 98.0%], 0.11 M cobalt(II) nitrate tetrahydrate [$Co(NO_3)_2 \cdot 6H_2O$, Samchun, 98.0%], 4 g PVP (Mw: 40,000, Samchun), 1.0 g acid-treated CNTs, and 10 g PS nanobeads, 100 nm in size, in 400 mL distilled water. A scheme for the spray pyrolysis process is shown in Scheme 1. The detailed procedure of the spray pyrolysis has been described in our previous work [24]. In order to obtain NiCoO/CNT hybrid microspheres as a precursor, spray pyrolysis was done at 700 °C with N_2 at 10 L min^{-1} flow rate. HYS-(NiCo)Se_2/CNT microspheres were finally obtained by simple selenization of the precursor powders at 450 °C under hydrogen selenide (H_2Se) vapor, generated by the reaction of selenium powders with hydrogen in a 5% mixed H_2/Ar gas atmosphere.

2.2. Characterization techniques

The microstructure of HYS-(NiCo)Se_2/CNT microspheres was observed by field-emission scanning electron microscopy (Ultra Plus, Zeiss) and field-emission TEM (JEOL, JEM-2100F). Phase analysis was done by XRD (Bruker D8 Discover with GADDS) using Cu Kα radiation (λ = 1.5418 Å). An XPS instrument (Thermo Scientific, K-Alpha) with focused monochromatic Al Kα radiation at 12 kV and 20 mA was used to analyze the composition of the sample. The surface area of HYS-(NiCo)Se_2/CNT microspheres was measured by the BET method using N_2 as the adsorbate gas. TGA was done using a thermogravimetric analyzer (Pyris 1 TGA, Perkin–Elmer) in the temperature range of 25–700 °C at a heating rate of 10 °C min^{-1} in air.

2.3. Electrochemical measurements

The electrochemical properties of HYS-(NiCo)Se_2/CNT microspheres were measured by constructing 2032-type coin cells. The cell electrode composed of active material, conductive black carbon (Super-P), and sodium carboxymethyl cellulose (CMC) as a binder in a mass ratio of 7:2:1. The working electrodes were formed by coating the slurry onto copper foils, which were subsequently dried at 70 °C for 3 h. A Na metal and porous polypropylene (PP) film were used as the counter electrode and separator, respectively. The electrolyte consisted of 1.0 M sodium trifluoromethanesulfonate

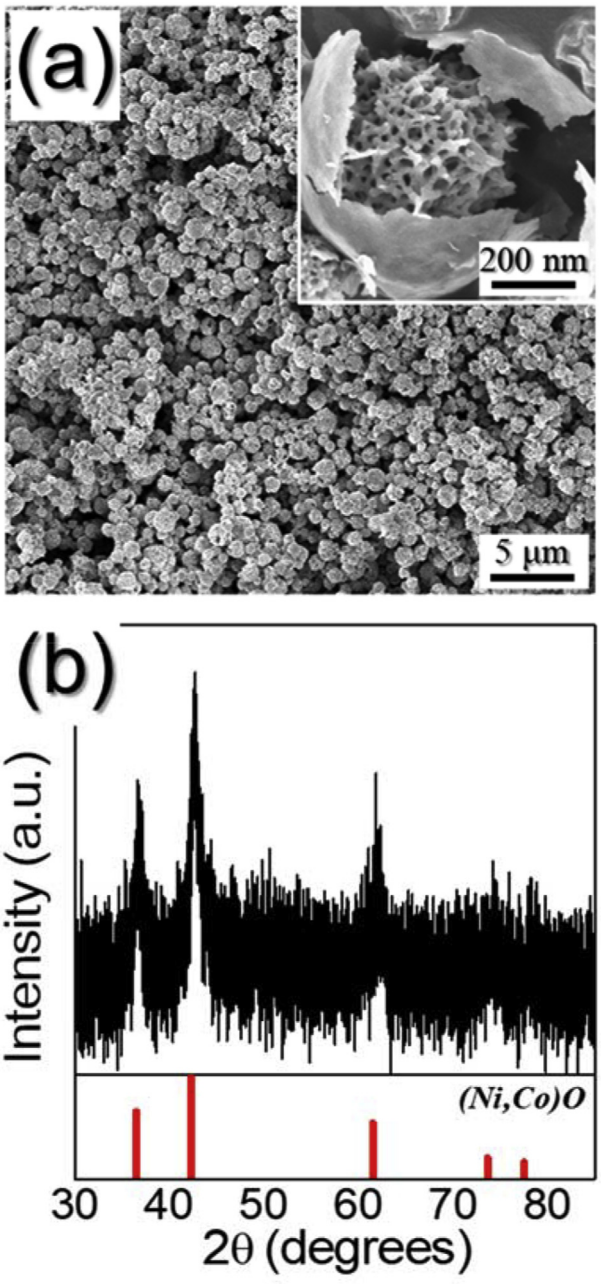

Fig. 1. Morphologies and XRD pattern of the as-prepared precursor (NiCo)O/CNT hybrid microspheres.

($NaCF_3SO_3$) in diethylene glycol dimethyl ether (DEGDME). The coin cell was assembled at room temperature in an Ar-filled glove box where water and oxygen concentration was kept at less than 1 ppm. The discharge–charge characteristics of the samples were measured at various current densities in the voltage range of 0.3–2.9 V. Cyclic voltammetry measurements were done at a scan rate of 0.1 mV s^{-1}. The dimensions of the anode were 1.4 cm × 1.4 cm, and the mass loading was approximately 0.8 mg cm^{-2}. The electrochemical impedance was measured by EIS over a frequency range of 0.01 Hz–100 KHz with a signal amplitude of 10 mV.

3. Results and discussion

The hierarchical yolk-shell-structured $NiCoSe_2$/CNT [HYS-(NiCo)Se_2/CNT] hybrid microspheres were prepared by one-step spray pyrolysis and subsequent selenization heat treatment. For this, the precursor powders of (NiCo)O/CNT hybrid microspheres were first obtained via spray pyrolysis from a spray solution by applying the mechanism of phase separation between PVP and PS colloidal nanobeads. The metal salts were transformed to NiO, CoO solid solution below 300 °C. The decomposition of the size-controlled PS nanobeads (~100 nm) in the droplet during spray pyrolysis above 450 °C and subsequent thermal contraction of the inner part of the composite during the spray pyrolysis formed a hollow space between yolk and shell. In particular, the yolk of the composite has a porous structure with walls linked with CNTs. The procedure for the formation of HYS-(NiCo)Se_2/CNT microspheres via simple selenization at 400 °C during 12 h of the precursor powders obtained after spray pyrolysis is described in Scheme 2. Direct selenization at of the precursor powders resulted in the formation of the (Ni,Co)Se_2/CNT hybrid microspheres with hierarchical yolk–shell structure, which were formed by conversion of (NiCo)O in the precursor powders into the (Ni,Co)Se_2 phase.

The morphology and phase analysis of the (NiCo)O/CNT hybrid microspheres as a precursor obtained after spray pyrolysis are

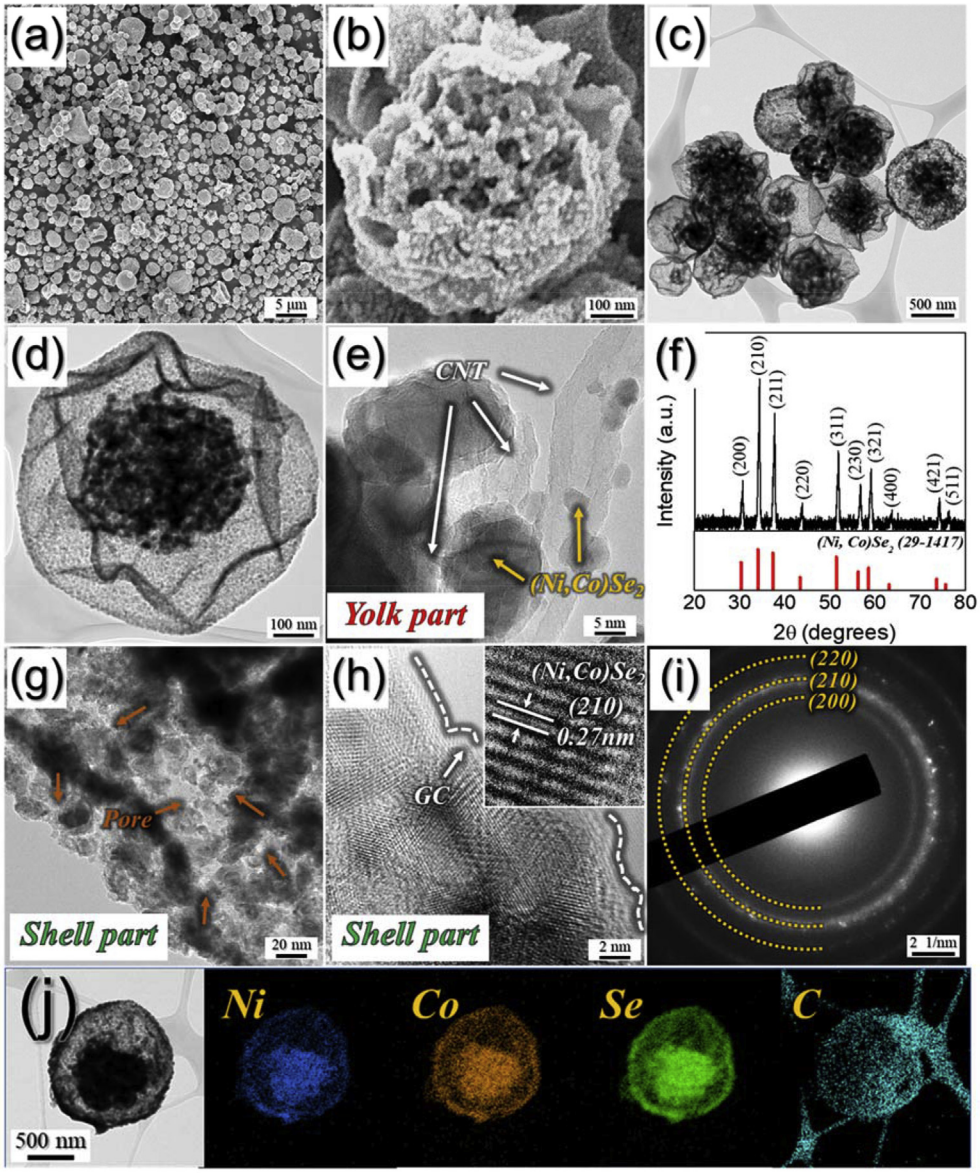

Fig. 2. Morphologies, SAED, XRD patterns, and elemental mapping images of HYS-(NiCo)Se_2/CNT microspheres: (a,b) FE-SEM, (c,d) TEM, (e,g,h) HR-TEM images, (f) XRD pattern, (i) SAED pattern, and (j) elemental mapping images.

shown in Fig. 1. The powders showed the hierarchical yolk–shell structure with distinct yolk@void@shell configuration as shown in the fractured in-set FE-SEM image in Fig. 1a. In particular, the yolk part showed a porous structure formed by PS decomposition during the spray pyrolysis. The obtained precursor powders were composed with low-crystalline (NiCo)O crystals and CNTs, as confirmed by the XRD result in Fig. 1b.

HYS-(NiCo)Se_2/CNT microspheres obtained by simple selenization of the precursor powders at 450 °C are shown in Fig. 2. Even after selenization, the unique hierarchical yolk-shell structure was well maintained, as shown in the FE-SEM and TEM images in Fig. 2a–d. In addition, the HYS-(NiCo)Se_2/CNT microspheres had a configuration of an external embossed thin shell, inside porous yolk, and an interstitial hollow space. From the enlarged yolk part in Fig. 2e, CNT walls and (Ni,Co)Se_2 nanoparticles anchored to CNTs constituted the porous yolk, in which the phase of (Ni,Co)Se_2 was confirmed by the XRD result in Fig. 2f. The mean crystallite size of the (Ni,Co)Se_2 nanocrystals calculated from the half-width of the (210) peak using the Scherrer equation was 21.8 nm, which is in good accordance with the size of the formed (Ni,Co)Se_2 nanoparticles observed in the TEM images (Fig. 2e,g). The external embossed thin shell of HYS-(NiCo)Se_2/CNT microspheres is also composed of (Ni,Co)Se_2 nanocrystals and numerous pores between nanoparticles, as indicated by arrows in the detailed shell-part image in Fig. 2g. In particular, graphitic carbon (GC) surrounding the (Ni,Co)Se_2 nanoparticles was formed, as shown in Fig. 2h. During the selenization, the amorphous carbon (AC) decomposed from PVP was graphitized under the influence of the Ni and Co metals acting as catalysts. Since the activation energy of the AC to GC conversion could be lowered by the catalysts, graphitization

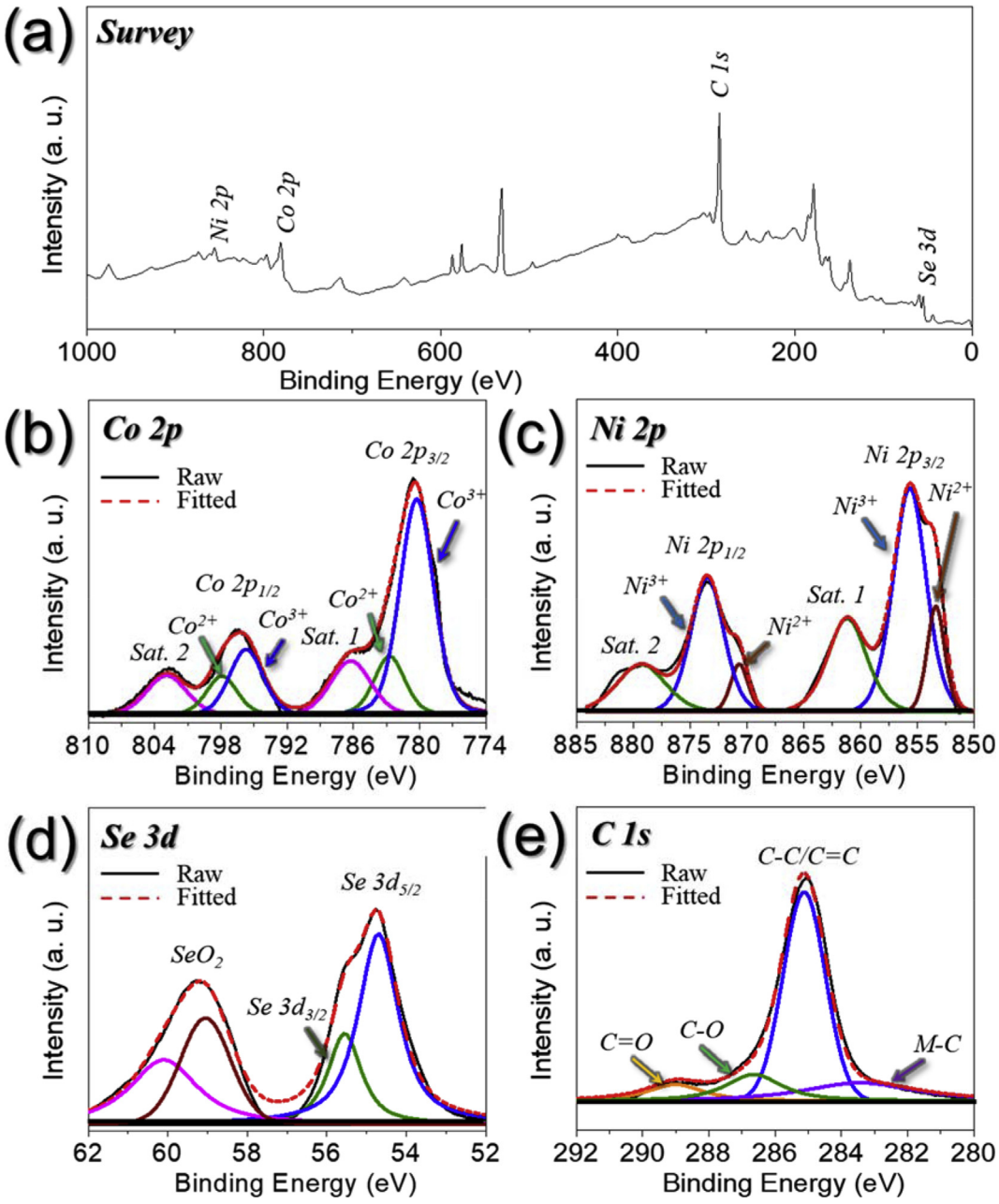

Fig. 3. Characteristics of HYS-(NiCo)Se_2/CNT microspheres: (a) XPS survey spectrum, (b) Co 2p XPS spectrum, (c) Ni 2p XPS spectrum, (d) Se 3d XPS spectrum, (e) C 1s XPS spectrum.

occurred at a relatively low temperature of 450 °C [18]. The high-resolution inset TEM image in Fig. 2h exhibits the lattice fringes separated by 0.27 nm, which reveals the existence of the (210) plane of (Ni,Co)Se_2 nanocrystals [26]. The selected-area electron diffraction (SAED) pattern further elucidates the formation of (Ni,Co)Se_2 nanoparticles after selenization in Fig. 2i. The elemental-mapping images shown in Fig. 2j show the uniform distribution of Ni, Co, Se, and C in the composite, which proves the complete transformation of (NiCo)O into (Ni,Co)Se_2 crystals in the composite by simple selenization.

The chemical nature of the HYS-(NiCo)Se_2/CNT microspheres was analyzed by XPS, as shown in Fig. 3. The XPS survey scan revealed the peaks confirming the existence of Ni, Co, C, and Se (Fig. 3a). In the XPS spectrum of Co 2p in Fig. 3b, the Co $2p_{1/2}$ and Co $2p_{3/2}$ peaks were deconvoluted into peaks located at 780.1 and 795.4 eV for Co^{3+}, and 782.4 and 797.8 eV for Co^{2+} [26,27]. Additionally, the Ni 2p XPS spectrum in Fig. 3c was also deconvoluted into peaks located at 855.7 and 873.5 eV for Ni^{3+}, and 853.3 and 870.4 eV for Ni^{2+} [28,29]. These results indicate that the HYS-(NiCo)Se_2/CNT microspheres are composed of Co^{3+}, Co^{2+}, Ni^{3+}, and Ni^{2+}, as is in good agreement with previous literature for the phase of (Ni,Co)Se_2 [22]. Additionally, the peaks at 853.3 eV for Ni^{2+}, 855.7 eV for Ni^{3+}, 782.4 eV for Co^{2+}, and 795.4 eV for Co^{3+} include NiO, Ni_2O_3, CoO, and Co_3O_4 phases could be formed by surface oxidation of HYS-(NiCo)Se_2/CNT microspheres to an air atmosphere [30,31]. In the Se 3d spectrum in Fig. 3d, the peaks located at 55.5 and 54.6 eV correspond to the binding energies of Se $3d_{3/2}$ and Se $3d_{5/2}$, respectively, which also originate from the (Ni,Co)Se_2 phase. The additional Se–O peaks at 59.1 and 60.3 eV are attributed to the selenium oxide because of the exposure of HYS-(NiCo)Se_2/CNT microspheres to an air atmosphere [32–34]. The C 1s spectrum in Fig. 3e shows four deconvoluted peaks corresponding to M(metal)-C, C–C/C=C, C–O, and, C=O at 283.3, 285.0, 286.6, and 289.0 eV, respectively [6,35]. The peak for the C–C/C=C bond exhibits the highest intensity, and those corresponding to the C–O and C=O bonds exhibit particularly low intensities, indicating the thermal reduction of the oxidized CNTs and formation of GC from AC during selenization. The peak at 283.3 eV for the M – C bond is attributed to the bonding with binary Co and Ni metals and carbonaceous materials in the HYS-(NiCo)Se_2/CNT microspheres [6].

The TG curve of the HYS-(NiCo)Se_2/CNT microspheres is shown in Fig. 4a. The first weight increase observed at around 250 °C results from the decomposition of (Ni,Co)Se_2 crystals into NiO_x, CoO_x, and SeO_2. The following weight loss at around 380 °C results from both carbon combustion and decomposition of SeO_2. However, the weight loss of the sample was slightly diminished by the oxidation of $CoSe_2$ into $CoSeO_4$ and SeO_2. The final weight decrease between 450 and 570 °C is attributed to both the further decomposition of $CoSeO_4$ into Co_3O_4, $NiSeO_4$ and Ni_2O_3 into NiO, and the continuous decomposition of SeO_2 in the composite. On the basis of the TG analysis and elemental analysis (EA) in Table 1, the carbonaceous materials, including CNTs and GC contents in the HYS-(NiCo)Se_2/CNT microspheres, is approximately 5.1 wt %. The Brunauer-Emmett-Teller (BET) surface area of the HYS-(NiCo)Se_2/CNT microspheres was calculated as 28.7 $m^2 g^{-1}$ in Fig. 4b.

The carbon of HYS-(NiCo)Se_2/CNT microsphere was characterized by Raman spectroscopy. The degree of graphitization of the C material can be evaluated according to the ratio of the peak intensity of the D-band to that of the G-band (I_D/I_G) [36]. The I_D/I_G

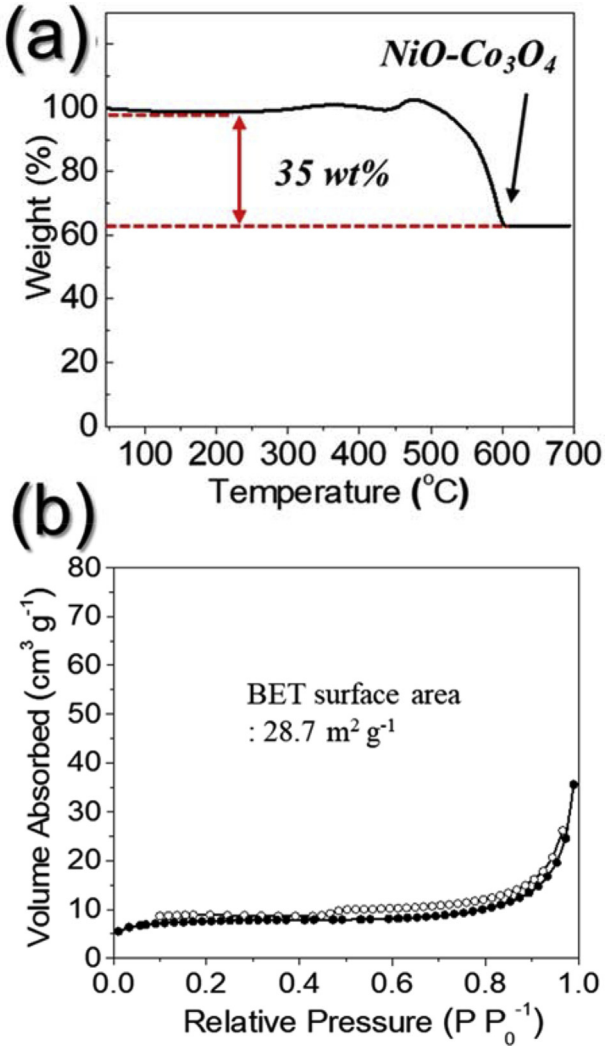

Fig. 4. (a) TG curve and (b) N_2 adsorption-desorption isotherms microspheres measured at 77 K of HYS-(NiCo)Se_2/CNT.

Table 1
Elemental analysis HYS-(NiCo)Se_2/CNT microspheres.

Sample	Carbon (wt%)
HYS-(NiCo)Se_2/CNT microspheres	5.1

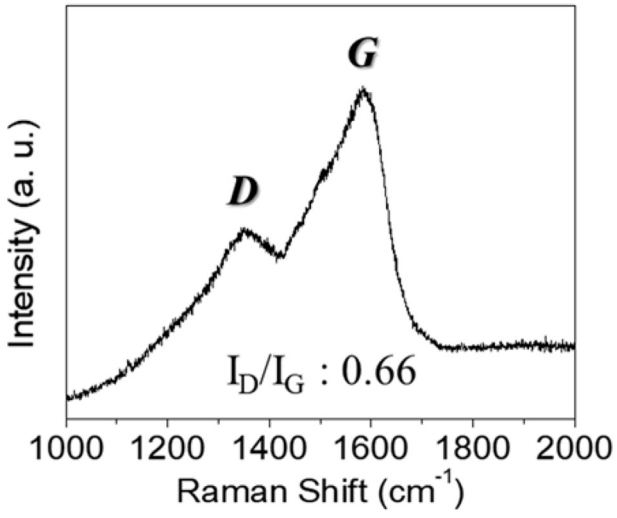

Fig. 5. Raman spectrum of HYS-(NiCo)Se_2/CNT microspheres.

ratio for the HYS-(NiCo)Se_2/CNT microsphere was 0.66. The highly ordered CNTs in HYS-(NiCo)Se_2/CNT microsphere contributed to the high intensity of the G-band (Fig. 5).

The electrochemical properties of the HYS-(NiCo)Se_2/CNT microspheres for sodium-ion storage were investigated via cyclic voltammetry (CV) and galvanostatic charge/discharge tests in the potential range of 0.3–2.9 V *vs.* Na^+/Na. The cyclic voltammograms of the HYS-(NiCo)Se_2/CNT microspheres during 20 cycles at a scan rate of 0.1 mV s^{-1} are shown in Fig. 6a. In the first cathodic scan, the HYS-(NiCo)Se_2/CNT microspheres exhibited a peak at 1.01 V, which is attributed to the reduction of (Ni,Co)Se_2 into metallic Ni and Co [25]. In the first charge scan, both a shoulder peak at 1.81 V and a peak at 1.89 V indicate the re-combination of each metallic Ni and Co nanograin with Se [25]. In the second cycle, the cathodic peak shifted to higher potentials at 1.45 V, because of the formation of ultrafine nanocrystals during the Na-ion insertion and desertion during the first cycle [22,37,38]. The formation of ultrafine nanocrystals increases the active sites of the host material so that the peak is shifted to a higher potential after the first discharging process [22,37,38]. The intensities of the peaks at 1.45 V (in cathodic scan) and at 1.89 V (in anodic scans) gradually decreased during later cycles. Along with this, the peaks at 1.62 V, 0.63 V (in the cathodic scans), 1.53 V, and 2.01 V (in the anodic scans) increased gradually because of formation of NiSe, CoSe, and Na_2Se crystals from the initial (Ni,Co)Se_2 nanocrystals as cycles proceeded [39,40]. Therefore, the peaks at 1.62 V and 0.63 V in the cathodic scans from the second cycle onward are attributed to the reduction of CoSe to metallic Co and the formation of Li_2Se (Na_2Se) [39]. The peaks at 1.53 V and 2.01 V in the anodic scan are attributed to the conversion of metallic Co with Se [39]. The results are in good agreement with the previous literature for each conversion reaction of $NiSe_2$ or $CoSe_2$ in SIBs [41,42].

The discharge and charge profiles of the HYS-(NiCo)Se_2/CNT microspheres at a high current density of 3.0 A g^{-1} are shown in Fig. 6b. The plateaus coincided well with the CV results described above. The long plateau at 1.2 V during the 1st discharge is attributed to the reduction of (Ni,Co)Se_2 into metallic Ni and Co, and the plateau at 1.8 V in the 1st charge process results from re-combination of metallic Ni and Co nanograins with Se. From the second cycle onward, plateaus at 1.6 V, 1.2 V, and 0.7 V were newly observed as confirmed from the CV result, which is caused by the phase transformation of (Ni,Co)Se_2 into CoSe, NiSe, and Na_2Se. The discharge capacities of the HYS-(NiCo)Se_2/CNT microspheres for the 1st, 5th, 10th, and 20th cycles were 512, 468, 455, and 448 mA h g^{-1}, respectively; their corresponding Coulombic efficiencies were 76.2, 99.1, 99.5, and 99.6%, respectively. The initial

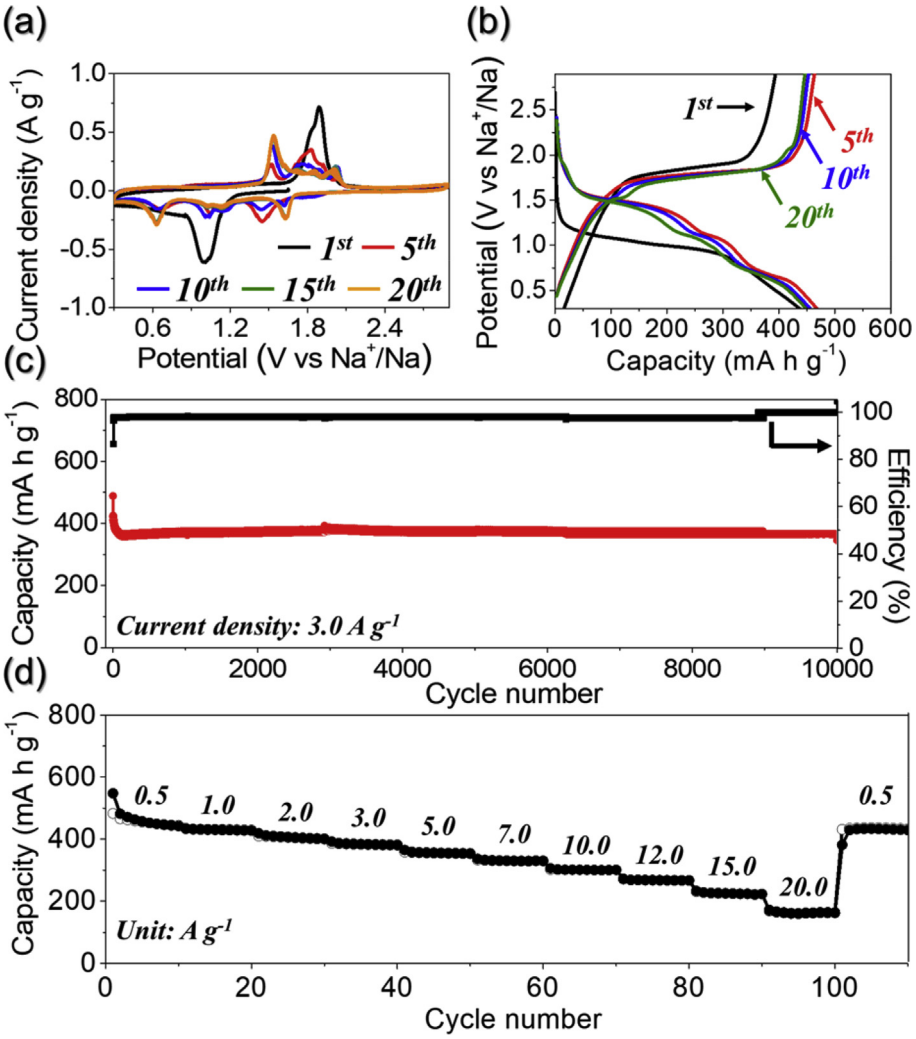

Fig. 6. Electrochemical properties of HYS-(NiCo)Se_2/CNT microspheres: (a) CV curves, (b) charge-discharge profiles, (c) cyclic performance at a current density of 3.0 A g^{-1}, and (d) rate performance.

loss of capacity is due to irreversible processes, such as irreversible trapping of Na^+ ions in the (Ni,Co)Se_2 crystal lattice, which involves the formation of a solid electrolyte interface (SEI) and electrolyte decomposition. However, the HYS-(NiCo)Se_2/CNT microspheres exhibited high Coulombic efficiencies of above 99.0% from the 5th cycle onward at a high current density of 3.0 A g^{-1}.

The long-term cycle property of the HYS-(NiCo)Se_2/CNT microspheres at a high current density of 3.0 A g^{-1} is shown in Fig. 6c. The discharge capacity of the microspheres was maintained steady over 10,000 cycles. The discharge capacity of the microspheres was 366 mA h g^{-1} after 10,000 cycles, and their capacity retention after the 2nd cycle was 85%. In this study, the synergistic effects of the uniquely hierarchical yolk-shell structure, CNTs walls with interstitial mesopores, and graphitic carbon surrounding the (Ni,Co)Se_2 nanoparticles effectively buffer the pressure from the contraction or expansion of the (Ni,Co)Se_2 active materials during the repeated charge, which resulted in high structural stability during the cycles and the excellent cycle performance of the HYS-(NiCo)Se_2/CNT microspheres. The rate performance of the HYS-(NiCo)Se_2/CNT microspheres at current densities from 0.5 to 20.0 A g^{-1} is shown in Fig. 6d. The HYS-(NiCo)Se_2/CNT microspheres showed excellent rate performance even at high current densities. The microspheres had final discharge capacities of 444, 429, 400, 380, 352, 329, 300, 266, 222, and 163 mA h g^{-1} at current densities of 0.5, 1.0, 2.0, 3.0, 5.0, 7.0, 10.0, 12.0, 15.0 and 20.0 A g^{-1}, respectively. In addition, the capacities recovered well to 428 mA h g^{-1} when the current density was returned to 0.5 A g^{-1} after cycling at high current densities. The unique nanostructure composed of a porous yolk with mesopores and an embossed porous thin shell enabled penetration of the liquid electrolyte into the microspheres, ensuring the facile diffusion of Na ions by shortening their diffusion path. Additionally, The CNTs walls composing the yolk and GC surrounding (Ni,Co)Se_2 nanoparticles contributed to the high electrical conductivity of the microspheres, which facilitates fast electron transfer by improving electrical contact between the active sites and the electrode. These synergistic effects resulted in the high rate property of the microspheres.

The superior Na-ion storage property of the HYS-(NiCo)Se_2/CNT microspheres was further verified using electrochemical impedance spectroscopy (EIS) measurements before and after cycles in a fully charged state [43–45]. The Nyquist plots obtained by deconvolution with Randle-type equivalent circuit models before and after cycling (Fig. 7a and b) are shown in Fig. 7c and d. The compressed semicircles in the medium-frequency range describe the charge-transfer resistance (R_{ct}) of the electrode. The synergistic effects of the mesoporous yolk with CNTs walls with high electrical conductivity, embossed porous thin shells, and the anchored (Ni,Co)Se_2 nanoparticles resulted in high structural stability during the cycles, therefore it had low R_{ct} value of 162 Ω prior to cycling. The HYS-(NiCo)Se_2/CNT microspheres had low R_{ct} values of 4.0 Ω, 4.2 Ω, and 6.1 Ω even after the 3rd, 30th, and 100th cycles, respectively in Fig. 6b, which proves the continuous high structural stability of the HYS-(NiCo)Se_2/CNT microspheres during repeated cycles. In order to prove the structure stability of HYS-(NiCo)Se_2/CNT microspheres, the microstructure of the microspheres obtained after 100 cycles was investigated by FE-SEM in Fig. 8. As a result, the hierarchical microsphere structure was well maintained without broken particle even after 100 cycles at a high current density of 3.0 A g^{-1}. The result demonstrates the excellent structure stability of HYS-(NiCo)Se_2/CNT microsphere, leading to the superior cycle property of the cell, in this study.

4. Conclusions

Hierarchical yolk-shell-structured $NiCoSe_2$/CNT hybrid microspheres consisting of a porous yolk and embossed hollow thin shell were prepared by one-step spray pyrolysis and a subsequent selenization heat treatment. In particular, the porous yolk was made up of CNTs walls and anchored (Ni,Co)Se_2 nanoparticles. Additionally, graphitic C was formed surrounding the (Ni,Co)Se_2 nanoparticles

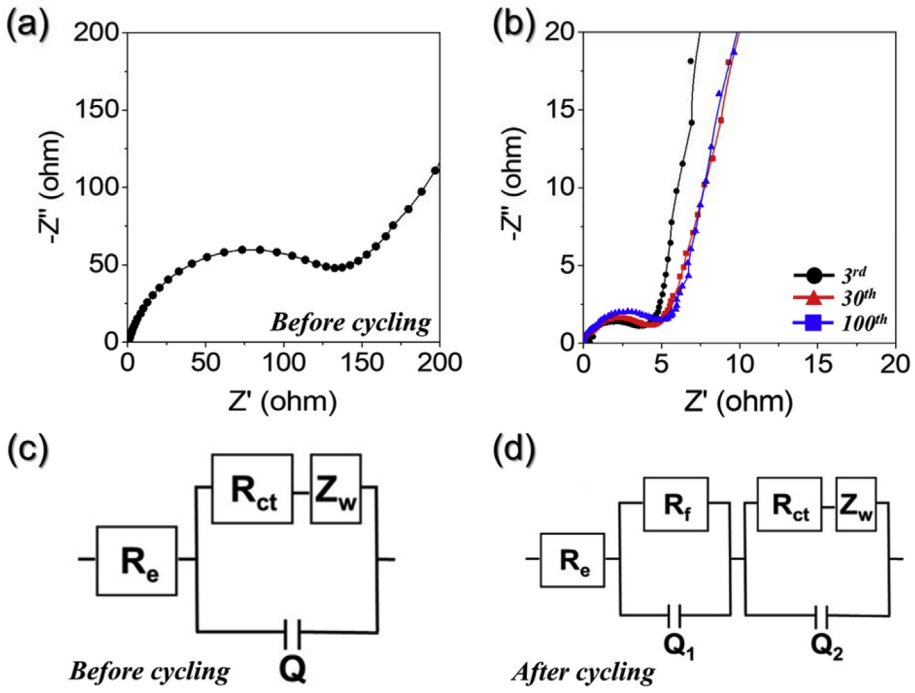

Fig. 7. (a,b) Nyquist impedance plots of HYS-(NiCo)Se_2/CNT microspheres for Na ion storage: (a) before cycling, (b) after 3, 30, and 100 cycles, (c,d) Equivalent circuit models used for AC impedance fitting: (c) before cycling, (d) after cycles, R_{ct} = charge-transfer resistance, R_e = electrolyte resistance, R_f = SEI layer resistance, Q_1 = dielectric relaxation capacitance, Q_2 = associated double layer capacitance.

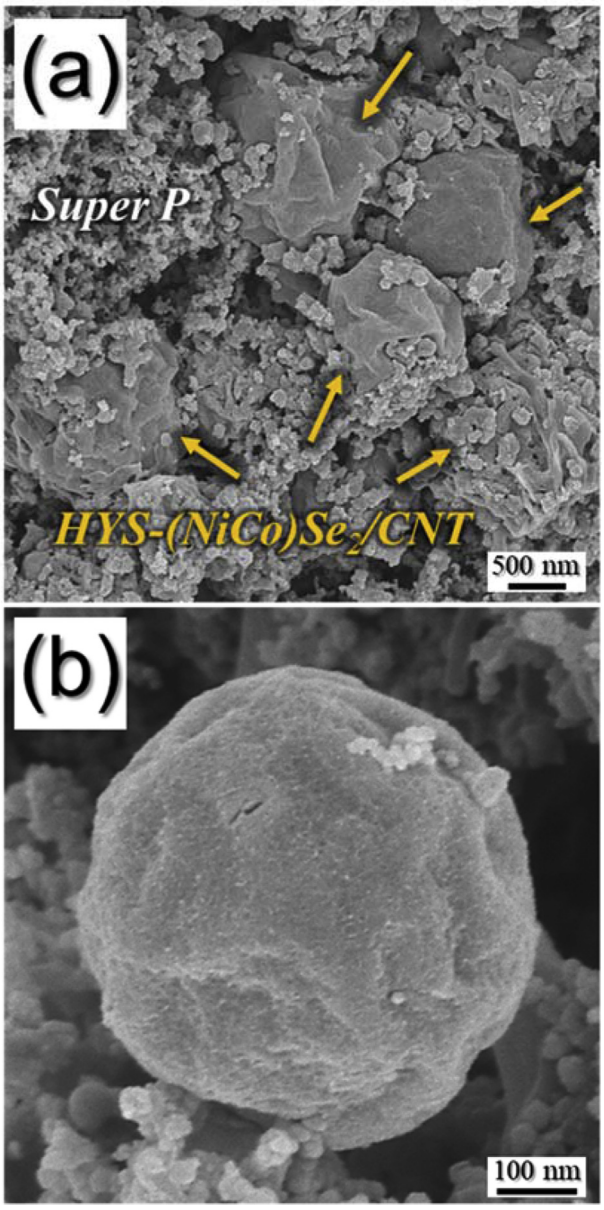

Fig. 8. Morphologies of HYS-(NiCo)Se_2/CNT microspheres obtained after 100 cycles: (a) low-magnification and (b) high-magnification FE-SEM images.

under the influence of the Ni and Co metals acting as catalysts for graphitization during selenization. The synergistic effects of the uniquely hierarchical yolk-shell structure, CNTs walls with interstitial mesopores, and graphitic carbon surrounding (Ni,Co)Se_2 nanoparticles effectively buffer the pressure from the contraction or expansion of the (Ni,Co)Se_2 active materials during the repeated charge, which resulted in high structural stability during the cycles and excellent cycle performance of the HYS-(NiCo)Se_2/CNT microspheres. In addition, the porous yolk with mesopores and embossed porous thin shell enabled penetration of the liquid electrolyte into the microspheres, ensuring the facile diffusion of Li ions by shortening their diffusion path. The CNTs walls composing the yolk and the GC surrounding the (Ni,Co)Se_2 nanoparticles contribute to the high electrical conductivity of the HYS-(NiCo)Se_2/CNT microspheres, which facilitates fast electron transfer by improving electrical contact between the active sites and the electrode. These synergistic effects resulted in the excellent sodium-ion storage performance of the HYS-(NiCo)Se_2/CNT microspheres.

Acknowledgements

This work was supported by the National Research Foundation of Korea (NRF) grant funded by the Korea government (MSIP) (NRF-2018R1A4A1024691, NRF-2017M1A2A2087577, and NRF-2018R1D1A3B07042514).

Appendix A. Supplementary data

Supplementary data to this article can be found online at https://doi.org/10.1016/j.jallcom.2019.07.351.

References

[1] X. Ou, J. Li, F. Zheng, P. Wu, Q. Pan, X. Xiong, C. Yang, M. Liu, *In situ* X-ray diffraction characterization of $NiSe_2$ as a promising anode material for sodium ion batteries, J. Power Sources 343 (2017) 483–491.
[2] S.-K. Park, J.K. Kim, Y.C. Kang, Excellent sodium-ion storage performances of $CoSe_2$ nanoparticles embedded within N-doped porous graphitic carbon nanocube/carbon nanotube composite, Chem. Eng. J. 328 (2017) 546–555.
[3] K. Zhang, Z. Hu, X. Liu, Z. Tao, J. Chen, $FeSe_2$ microspheres as a high-performance anode material for Na-ion batteries, Adv. Mater. 27 (2015) 3305–3309.
[4] Y. Fang, X.Y. Yu, X.W. Lou, Formation of hierarchical Cu-doped $CoSe_2$ microboxes via sequential ion exchange for high-performance sodium-Ion batteries, Adv. Mater. 30 (2018), 1706668.
[5] Z. Hu, L. Wang, K. Zhang, J. Wang, F. Cheng, Z. Tao, J. Chen, MoS_2 nanoflowers with expanded interlayers as high-performance anodes for sodium-ion batteries, Angew. Chem. Int. Ed. 53 (2014) 12794–12798.
[6] S.Y. Jeong, S.-K. Park, Y.C. Kang, J.S. Cho, One-dimensional nanostructure comprising $MoSe_2$ nanosheets and carbon with uniformly defined nanovoids as an anode for high-performance sodium-ion batteries, Chem. Eng. J. 351 (2018) 559–568.
[7] S.Y. Jeong, S. Ghosh, J.-K. Kim, D.-W. Kang, S.M. Jeong, Y.C. Kang, J.S. Cho, Multi-channel-contained few-layered $MoSe_2$ nanosheet/N-doped carbon hybrid nanofibers prepared using diethylenetriamine as anodes for high-performance sodium-ion batteries, J. Ind. Eng. Chem. 75 (2019) 100–107.
[8] F. Niu, J. Yang, N. Wang, D. Zhang, W. Fan, J. Yang, Y. Qian, $MoSe_2$-covered N,P-doped carbon nanosheets as a long-life and high-rate anode material for sodium-ion batteries, Adv. Funct. Mater. 27 (2017) 1700522.
[9] F. Zhang, C. Xia, J. Zhu, B. Ahmed, H. Liang, D.B. Velusamy, U. Schwingenschlögl, H.N. Alshareef, $SnSe_2$ 2D anodes for advanced sodium ion batteries, Adv. Energy Mater. 6 (2016) 1601188.
[10] J.S. Cho, J.-K. Lee, Y.C. Kang, Graphitic carbon-coated $FeSe_2$ hollow nanosphere-decorated reduced graphene oxide hybrid nanofibers as an efficient anode material for sodium ion batteries, Sci. Rep. 6 (2016) 23699.
[11] J.S. Cho, S.Y. Lee, Y.C. Kang, First introduction of $NiSe_2$ to anode material for sodium-ion batteries: a hybrid of graphene-wrapped $NiSe_2$/C porous nanofiber, Sci. Rep. 6 (2016) 23338.
[12] Z. Zhang, X. Shi, X. Yang, Y. Fu, K. Zhang, Y. Lai, J. Li, Nanooctahedra particles assembled $FeSe_2$ microspheres embedded into sulfur-doped reduced graphene oxide sheets as a promising anode for sodium ion batteries, ACS Appl. Mater. Interfaces 8 (2016) 13849–13856.
[13] F. Zhao, S. Shen, L. Cheng, L. Ma, J. Zhou, H. Ye, N. Han, T. Wu, Y. Li, J. Lu, Improved sodium-ion storage performance of ultrasmall iron selenide nanoparticles, Nano Lett. 17 (2017) 4137–4142.
[14] J.S. Cho, J.-S. Park, K.M. Jeon, Y.C. Kang, 1-D nanostructure comprising porous Fe_2O_3/Se composite nanorods with numerous nanovoids, and their electrochemical properties for use in lithium-ion batteries, J. Mater. Chem. 5 (2017) 10632–10639.
[15] J.-S. Park, S.Y. Jeong, K.M. Jeon, Y.C. Kang, J.S. Cho, Iron diselenide combined with hollow graphitic carbon nanospheres as a high-performance anode material for sodium-ion batteries, Chem. Eng. J. 339 (2018) 97–107.
[16] C. Wu, Y. Jiang, P. Kopold, P.A. van Aken, J. Maier, Y. Yu, Peapod-like carbon-encapsulated cobalt chalcogenide nanowires as cycle-stable and high-rate materials for sodium-ion anodes, Adv. Mater. 28 (2016) 7276–7283.
[17] M.S. Jo, S. Ghosh, S.M. Jeong, Y.C. Kang, J.S. Cho, Coral-like yolk–shell-structured nickel oxide/carbon composite microspheres for high-performance Li-ion storage anodes, Nano-Micro Lett. 11 (2019) 3.
[18] J.S. Cho, J.M. Won, J.-K. Lee, Y.C. Kang, Design and synthesis of multiroom-structured metal compounds–carbon hybrid microspheres as anode materials for rechargeable batteries, Nano Energy 26 (2016) 466–478.
[19] P. Ge, H. Hou, S. Li, L. Yang, X. Ji, Tailoring rod-like $FeSe_2$ coated with nitrogen-doped carbon for high-performance sodium storage, Adv. Funct. Mater. 28 (2018), 1801765.
[20] Y. Zhang, A. Pan, L. Ding, Z. Zhou, Y. Wang, S. Niu, S. Liang, G. Cao, Nitrogen-doped yolk–shell-structured CoSe/C dodecahedra for high-performance sodium ion batteries, ACS Appl. Mater. Interfaces 9 (2017) 3624–3633.

[21] C. Yuan, H.B. Wu, Y. Xie, X.W.D. Lou, Mixed transitional-metal oxides: design, synthesis, and energy-related applications, Angew. Chem. Int. Ed. 53 (2014) 1488–1504.
[22] Y.-Y. Huang, L.-Y. Lin, Synthesis of ternary metal oxides for battery-supercapacitor hybrid devices: influences of metal species on redox reaction and electrical conductivity, ACS Appl. Mater. Interfaces 1 (2018) 2979–2990.
[23] S.H. Oh, M.S. Jo, S.M. Jeong, Y.C. Kang, J.S. Cho, Hierarchical yolk-shell CNT-(NiCo)O/C microspheres prepared by one-pot spray pyrolysis as anodes in lithium-ion batteries, Chem. Eng. J. 368 (2019) 438–447.
[24] S.H. Choi, J.-K. Lee, Y.C. Kang, Controllable synthesis of yolk-shell-structured metal oxides with seven to ten components for finding materials with superior lithium storage properties, Nanoscale 6 (2014) 12421–12425.
[25] S.-K. Park, J.K. Kim, Y.C. Kang, Metal–organic framework-derived $CoSe_2$/(NiCo)Se_2 box-in-box hollow nanocubes with enhanced electrochemical properties for sodium-ion storage and hydrogen evolution, J. Mater. Chem. 5 (2017) 18823–18830.
[26] K. Ao, J. Dong, C. Fan, D. Wang, Y. Cai, D. Li, F. Huang, Q. Wei, Formation of yolk–shelled nickel–cobalt selenide dodecahedral nanocages from metal–organic frameworks for efficient hydrogen and oxygen evolution, ACS Sustain. Chem. Eng. 6 (2018) 10952–10959.
[27] H. Li, X. Qian, C. Zhu, X. Jiang, L. Shao, L. Hou, Template synthesis of $CoSe_2$/Co_3Se_4 nanotubes: tuning of their crystal structures for photovoltaics and hydrogen evolution in alkaline medium, J. Mater. Chem. 5 (2017) 4513–4526.
[28] Y. Du, G. Cheng, W. Luo, Colloidal synthesis of urchin-like Fe doped $NiSe_2$ for efficient oxygen evolution, Nanoscale 9 (2017) 6821–6825.
[29] J.-S. Park, Y.C. Kang, Multicomponent (Mo, Ni) metal sulfide and selenide microspheres with empty nanovoids as anode materials for Na-ion batteries, J. Mater. Chem. 5 (2017) 8616–8623.
[30] L. Zhai, C.H. Mak, J. Qian, S. Lin, S.P. Lau, Self- reconstruction mechanism in $NiSe_2$ nanoparticles/carbon fiber paper bifunctional electrocatalysts for water splitting, Electrochim, Acta 305 (2019) 37–46.
[31] K. Lan, J. Li, Y. Zhu, L. Gong, F. Li, P. Jiang, F. Niu, R. Li, Morphology enineering of $CoSe_2$ as efficient electrocatalyst for water splitting, J. Colloid Interface Sci. 539 (2019) 646–653.
[32] Y. Du, G. Cheng, W. Luo, $NiSe_2$/$FeSe_2$ nanodendrites: a highly efficient electrocatalyst for oxygen evolution reaction, Catal. Sci. Technol. 7 (2017) 4604–4608.
[33] P. Xiong, X. Ao, J. Chen, J.-G. Li, L. Lv, Z. Li, M. Zondode, X. Xue, Y. Lan, C. Wang, Nickel diselenide nanoflakes give superior urea electrocatalytic conversion, Electrochim. Acta 297 (2019) 833–841.
[34] J.-Y. Zhang, L. Lv, Y. Tian, Z. Li, X. Ao, Y. Lan, J. Jiang, C. Wang, Rational design of cobalt–iron selenides for highly efficient electrochemical water oxidation, ACS Appl. Mater. Interfaces 9 (2017) 33833–33840.
[35] S.H. Oh, J.K. Kim, Y.C. Kang, J.S. Cho, Three-dimensionally ordered mesoporous multicomponent (Ni, Mo) metal oxide/N-doped carbon composite with superior Li-ion storage performance, Nanoscale 10 (2018) 18734–18741.
[36] Y.J. Hong, J.S. Cho, Y.C. Kang, Superior electrochemical propertiees of nanofiber composed of hollow $CoFe_2O_4$ nanospheres covered with onion-like graphitic carbon, Chem. Eur J. 21 (2015) 18202–18208.
[37] Q. Wang, W. Zhang, C. Guo, Y. Liu, C. Wang, Z. Guo, In situ construction of 3D interconnected FeS@Fe_3C@graphitic carbon networks for high-performance sodium-ion batteries, Adv. Fucnt. Mater. 27 (2017), 1703390.
[38] Q. Li, J. Wu, J. Xu, V.P. Drabid, Synergistic sodation of cobalt oxide nanoparticles and conductive carbon nanotubes (CNTs) for sodium-ion batteries, J. Mater. Chem. 4 (2016) 8669–8675.
[39] Z. Ali, T. Tang, X. Huang, Y. Wang, M. Asif, Y. Hou, Cobalt selenide decorated carbon spheres for excellent cycling performance of sodium ion batteries, Energy Storage Mater 13 (2018) 19–28.
[40] Z. Zhang, X. Shi, X. Yang, Synthesis of core-shell NiSe/C nanospheres as anodes for lithium and sodium storage, Electrochim. Acta 208 (2016) 238–243.
[41] K. Zhang, M. Park, L. Zhou, G.H. Lee, W. Li, Y.M. Kang, J. Chen, Urchin-like $CoSe_2$ as a high-performance anode material for sodium-ion batteries, Adv. Funct. Mater. 26 (2016) 6728–6735.
[42] S. Zhu, Q. Li, Q. Wei, R. Sun, X. Liu, Q. An, L. Mai, $NiSe_2$ nanooctahedra as an anode material for high-rate and long-life sodium-ion battery, ACS Appl. Mater. Interfaces 9 (2016) 311–316.
[43] J. Jin, Z.-Q. Shi, C.-Y. Wang, Electrochemical performance of electrospun carbon nanofibers as free-standing and binder-free anodes for sodium-ion and lithium-ion batteries, Electrochim. Acta 141 (2014) 302–310.
[44] J.H. Lee, S.H. Oh, S.Y. Jeong, Y.C. Kang, J.S. Cho, Rattle-type porous Sn/C composite fibers with uniformly distributed nanovoids containing metallic Sn nanoparticles for high-performance anode materials in lithium-ion batteries, Nanoscale 10 (2018) 21483–21491.
[45] S.H. Oh, J.-S. Park, M.S. Jo, Y.C. Kang, J.S. Cho, Design and synthesis of tube-in-tube structured NiO nanobelts with superior electrochemical properties for lithium-ion storage, Chem. Eng. J. 347 (2018) 889–899.